



# Model tests on a floating coaxial-duct OWC wave energy converter with focus on the spring-like air compressibility effect

J.C.C. Portillo<sup>\*</sup>, J.C.C. Henriques, L.M.C. Gato, A.F.O. Falcão

IDMEC/LAETA, Instituto Superior Técnico, Universidade de Lisboa, Av. Rovisco Pais 1, 1049-001 Lisbon, Portugal

## ARTICLE INFO

### Keywords:

Wave energy  
Floating oscillating-water-column  
Coaxial-duct OWC  
Compressibility effects  
Physical model design  
Model testing

## ABSTRACT

The spring-like air compressibility effect in oscillating-water-column (OWC) wave energy converters may significantly affect the device's power performance. Yet, this effect has rarely been accounted for in physical model testing, especially in floating OWCs. Quantifying this effect in the development and analysis of OWCs is crucial for i) making better estimates of their performances and decreasing uncertainties, ii) improving design and testing processes, iii) reducing development costs, and iv) accelerating decision-making on wave energy projects. This paper presents experimental results of a floating coaxial-duct OWC at 1:40-scale. The experimental campaign comprised tests in which the Froude scale was applied to the whole converter structure and, for comparison, tests where the air chamber volume was expanded to comply with the aero-thermodynamic similitude. Tests included regular and irregular waves and various damping conditions. Experimental results show that compressibility effects can increase, decrease, or have neutral contributions to the mean absorbed power, depending on wave frequency. Another effect is the presence of reactive power. The capture width ratio is higher for the compressible experimental configuration in several cases. A new compressibility factor is proposed to aid in designing experimental and numerical campaigns.

## 1. Introduction

Sea waves are known to be a vast, practically untapped, renewable energy resource, especially for countries with coasts facing the open ocean [1,2]. Converting the waves into large-scale electrical energy has been a challenge, especially since the mid-1970s when the oil crisis of 1973 induced a major change in the renewable energies scenario. Since then, researchers and engineers have found that the wave-to-electrical energy conversion may be achieved, more or less efficiently, based on a wide variety of concepts [3–5]. The oscillating-water-column (OWC) was the first concept to be the object of significant development effort. More OWC prototypes have been deployed into the real sea than of any other type [6].

The OWC device is widely regarded as the simplest, most reliable, and extensively studied type of wave energy converter [6]. It consists of a partly submerged hollow structure, fixed or floating, with an opening below water level. The air trapped above the inner free-surface is alternately compressed and decompressed by wave action and is forced to flow through an air turbine that connects the air chamber to the atmosphere. The turbine is self-rectifying unless the converter is equipped with a rectifying valve system (which has been avoided except in very low power applications like navigation buoys). This

means that its rotational direction remains unchanged regardless of the air-flow direction. The axial-flow Wells turbine is the most popular self-rectifying air turbine since it was patented in 1976 [7–9]. However, other types of self-rectifying air turbines, of axial- and radial-flow types, have also been proposed [6,10–12], developed, and used, including variations with fixed and movable guide-vanes [13,14].

Most early full-sized OWC prototypes were isolated converters standing on, or near, the shoreline. A more promising topology integrates a row of OWC converters into a breakwater [15]. This allows the structure costs to be shared, and was done in Mutriku, Basque Country, Spain [16,17] and Civitavecchia, Italy [18].

However, if energy from the waves is to provide a significant contribution to the world electrical energy supply, the converters must be deployed over large areas of the ocean, i.e., floating converters in large arrays. Several types of floating OWCs have been proposed and developed [6]. Two should be mentioned here: the barge-shaped backward-bent-duct buoy (BBDB) [19,20] and the spar-buoy OWC [21]. Both reached the stage of prototype deployed and tested in the sea in the last four years: the IDOM Marmok A5 (of spar-buoy OWC type) in Basque Country, Spain, equipped with a 30 kW rated power biradial air

<sup>\*</sup> Corresponding author.

E-mail addresses: [juan.portillo@tecnico.ulisboa.pt](mailto:juan.portillo@tecnico.ulisboa.pt) (J.C.C. Portillo), [joaochenriques@tecnico.ulisboa.pt](mailto:joaochenriques@tecnico.ulisboa.pt) (J.C.C. Henriques), [luis.gato@tecnico.ulisboa.pt](mailto:luis.gato@tecnico.ulisboa.pt) (L.M.C. Gato), [antonio.falcao@tecnico.ulisboa.pt](mailto:antonio.falcao@tecnico.ulisboa.pt) (A.F.O. Falcão).

<https://doi.org/10.1016/j.energy.2022.125549>

Received 28 February 2022; Received in revised form 9 August 2022; Accepted 22 September 2022

Available online 27 September 2022

0360-5442/© 2022 The Author(s). Published by Elsevier Ltd. This is an open access article under the CC BY-NC-ND license (<http://creativecommons.org/licenses/by-nc-nd/4.0/>).

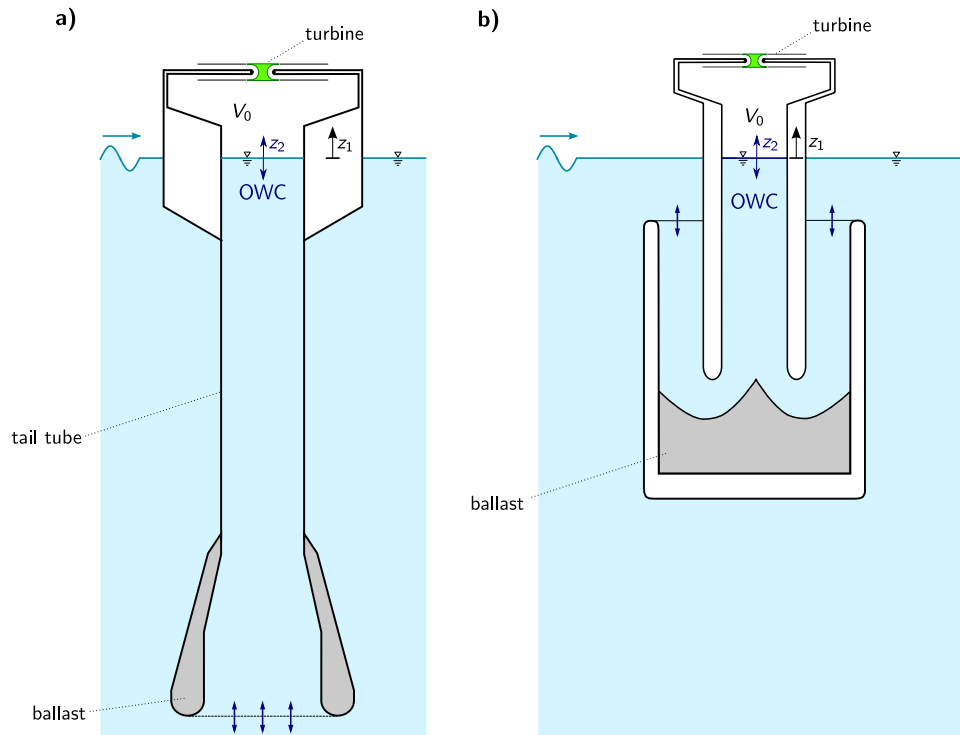


Fig. 1. Two OWC floating concepts: (a) Spar-buoy OWC and (b) CD-OWC.

turbine [22], and the OE35 (of BBDB type) deployed off Oahu island, Hawaii [23].

The present paper focuses on a new floating OWC concept: the coaxial-duct OWC converter (CD-OWC). The converter has a vertical axis of symmetry and consists essentially of two coaxial cylindrical ducts interconnected at their bottom ends (see Fig. 1). The outer duct is open to the sea at its top, whereas the inner duct extends above sea level and communicates with the atmosphere through a self-rectifying air turbine mounted at the top. An essential feature of the CD-OWC device is the small amplitude of its heaving oscillation under wave action. This is explained partially by the small waterplane area that results in a buoy with a low natural heave frequency that is weakly excited by the incoming waves. As such, the CD-OWC behaves in waves like a semisubmersible structure. Unlike the spar-buoy OWC, the CD-OWC opening to the outer water space is located closer to the sea surface, see Fig. 1, and the motion of the floater plays a minor role in the wave energy absorption process.

Experimental testing is an important process in developing wave energy converters (WECs) [24]. Since air is a compressible fluid, a spring-like effect in the OWC chamber may affect the whole energy conversion chain in OWC converters. Although this spring-like compressibility effect has been known from theoretical modelling since the mid-1980s [25], it has rarely been accounted for in fixed-model testing and even more rarely in the case of floating OWCs. If this effect is to be correctly reproduced in OWC model testing, the volume of the model air chamber must be oversized rather than simply following Froude's scaling law [25].

The experimental study of the spring-like air compressibility effect requires two sets of model tests to be performed in a wave tank: (i) with the air chamber scaled in the same way as the part of the structure subjected to wave action, and (ii) with an oversized air volume satisfying a theoretically derived scaling rule, which is normally done by connecting the model chamber to a rigid-walled additional reservoir of appropriate volume. Requirements (i) and (ii) were met in Ref. [26], where tests are reported on a quasi-two-dimensional fixed-structure OWC spanning a wave flume, which may be regarded as representing a long row of OWCs integrated into a rectilinear breakwater subject

to regular waves at normal incidence. It was found that, depending on incident wave frequency, the air compressibility may affect negatively or positively the power output level. A similar result was obtained in Refs. [27,28]. Another study, reported in Ref. [29], addressed a fully-three-dimensional fixed-structure OWC. The work involved experimentally validated results from a CFD code based on the numerical integration of the Reynolds-Averaged Navier–Stokes (RANS) equations coupled with an adequate turbulence model. The results showed that the volume of the air chamber (Froude scale and compressibility scale) could significantly affect the power performance of the converter.

Model tests of a CD-OWC at scale 1:40, in which the air compressibility effect was not accounted for, are reported in Ref. [24] for an isolated converter and in Ref. [30] for an array of five rigidly interconnected converters. One of those CD-OWC models was later tested in a different wave tank, complying with steps (i) and (ii) above to identify air compressibility effects. These tests are reported here.

The rest of the paper is divided into the following sections. Section 2 presents the theoretical modelling of compressibility in the air chamber of an OWC. Section 3 describes the material and experimental methods, and Section 4 presents the experimental results and their discussion. Finally, Section 5 summarises the most important conclusions.

## 2. Theoretical modelling and air chamber scaling

The spring-like air compressibility effect is a thermodynamic phenomenon associated with the dependence of density on pressure (and on temperature). This effect is significant in a full-sized OWC converter where the average air volume divided by the inner free-surface area is typically 3 to 8 m [31]. The ratio selection should be large enough to avoid ingestion of water by the air turbine under rough sea conditions. An increase in this ratio is not necessarily detrimental to the efficiency of the energy conversion [31]. Nevertheless, if the volume increases to very large values, the amplitude of the air pressure oscillations becomes very small, and the capability of the device to absorb wave energy vanishes. But, it is not simple to assess when the compressibility effects are significant, beneficial or detrimental, due to the dependency on the

specific hydrodynamic responses of OWC systems, their geometries, and the environmental conditions. This is further discussed in Section 4.6 where a new compressibility factor is presented.

From incident waves to turbine aerodynamic torque, the whole process is very complex. Its numerical modelling by CFD requires vast computational resources and computational time, and has rarely been attempted [32]. Instead, the turbine performance curves are usually known from model testing combined with dimensional analysis tools. The hydro- and thermodynamic modelling of the energy conversion chain in an OWC is outlined here, based on linear water wave theory.

Since the air in the chamber is partly renovated at each wave cycle, the inner air temperature is, on average, only a few degrees Celsius above atmospheric temperature. This explains why heat transfer across the chamber and turbine walls and the inner air–water interface may be neglected compared to the energy absorbed from the waves or absorbed by the turbine [25].

Three different scenarios may be considered for the flow through the turbine or, in the case of a model, the turbine simulator. (i) A perfectly efficient turbine, which, combined with the adiabatic assumption, implies specific entropy in the turbine and chamber equal to the atmospheric value. (ii) A realistically efficient turbine (Wells turbine or another type of self-rectifying turbine). (iii) An OWC model equipped with an orifice or porous plug to simulate a self-rectifying turbine of impulse type or a Wells turbine at a constant rotational speed, respectively. In cases (ii) and (iii), the specific entropy in the chamber exceeds the atmospheric value at all times; if assumed as spatially uniform, it remains constant during exhalation and may increase or decrease during inhalation.

It is convenient to consider separately the instantaneous values of the power available to the turbine,  $P_{\text{avai}}$ , and the turbine power output,  $P_{\text{out}}$ , such that  $P_{\text{out}} = \eta P_{\text{avai}}$ , where  $\eta$  is the instantaneous efficiency of the turbine. In case (ii) it is  $\eta < 1$  and in case (iii) it is  $\eta = 0$  (no work done). In both cases, the thermodynamic process in the turbine is strongly non-isentropic. Differently, for the air in the chamber, the specific entropy oscillates about an average value. In a numerical case study based on linear water wave modelling of a full-sized OWC converter equipped with a realistic Wells turbine, it was found that the isentropic approximation for the air in the chamber introduced an error not exceeding about 0.1% in the value of the power available to the turbine averaged over a time span of 980 s [25]. This approximation will be adopted in what follows. In Ref. [33], various approaches were examined in great detail theoretically including comparisons with experimental results, showing that the isentropic assumption provides a better model than the isothermal assumption does.

Let  $V$  be the time-dependent volume of the air chamber,  $\rho_a$  the air density, and  $m = \rho_a V$  the corresponding mass. The mass-flow rate of air through the turbine  $w_t = -dm/dt$  (positive for exhalation) is

$$w_t = \rho_a q - V \frac{d\rho_a}{dt}, \quad (1)$$

where  $q = -dV/dt$  is the volume flow rate displaced by the motion (or relative motion in the case of a floating OWC device) of the inner free surface. The second term on the right-hand side of Eq. (1) is proportional to the volume  $V$  and represents the effect of air compressibility.

In model testing, the Froude similarity criterion should be met for the part of the structure subject to wave action, but not for the air chamber size and the turbine or devices used to simulate it at a reduced scale. These issues are analysed here.

We consider a given OWC converter being model tested at (Froude) scale  $\lambda < 1$ . Eq. (1) represents the air mass balance in the chamber. If the dynamic similarity is to be kept, then the ratio between the two dimensionless terms on the right-hand side of the equation should take equal values in model and prototype, i.e.,  $Y_M^* = Y_F^*$ , where

$$Y^* = -\frac{V}{\rho_a q} \frac{d\rho_a}{dt}, \quad (2)$$

and subscripts “M” and “F” stand for model and full-size, respectively. If the thermodynamic process in the air chamber is approximately isentropic, as assumed above, and the air is considered as a perfect gas, Eq. (2) becomes

$$Y^* = -\frac{V}{q} \frac{1}{\gamma(p + p_{\text{atm}})} \frac{dp}{dt}, \quad (3)$$

where  $p_{\text{atm}}$  is atmospheric pressure,  $p + p_{\text{atm}}$  is the absolute air pressure in the chamber,  $\gamma = c_p/c_v$ , and  $c_p$  and  $c_v$  are the specific heat at constant pressure and constant volume, respectively.

Condition  $Y_M^* = Y_F^*$  (see above) implies that

$$\frac{V_M}{V_F} = \frac{q_M}{q_F} \frac{p_M + p_{\text{atm},M}}{p_F + p_{\text{atm},F}} \left( \frac{dp}{dt} \right)_F \left( \frac{dp}{dt} \right)_M^{-1}. \quad (4)$$

However, Froude similarity requires that (see Ref. [31])

$$\frac{q_M}{q_F} = \lambda^{5/2}, \quad \frac{p_M}{p_F} = \delta \lambda, \quad \left( \frac{dp}{dt} \right)_M = \delta \lambda^{1/2} \left( \frac{dp}{dt} \right)_F, \quad (5)$$

where  $\delta = \rho_{w,M}/\rho_{w,F}$  and  $\rho_w$  is water density; and  $\delta = 1/1.025$  or  $\delta = 1$  depending on whether the model is tested in freshwater or seawater. If Froude scale  $\lambda$  is to apply approximately to the air chamber volume, more precisely if  $V_M/V_F = \lambda^3$ , then it must be

$$p_{\text{atm},M} = p_{\text{atm},F} \delta \lambda. \quad (6)$$

Condition (6) is practically unfeasible if the Froude scale  $\lambda$  is not close to unity. The alternative is to neglect the pressure oscillations  $p_F$  in the chamber of the prototype in comparison with the atmospheric pressure  $p_{\text{atm},F}$ . Assuming  $p_{\text{atm},M} = p_{\text{atm},F}$ , the scale for the chamber volume becomes

$$\frac{V_M}{V_F} = \delta^{-1} \lambda^2. \quad (7)$$

Condition (7) (with  $\delta = 1$ ) was established for the first time and in a more restrictive way in Ref. [34].

### 3. Material and methods

#### 3.1. Experimental campaign plan and objective

The objective of the experiments reported here was to study the effects on power performance of compressibility in the air chamber of a CD-OWC converter at the Froude scale  $\lambda = 1/40$ . Two sets of experiments were performed. In one set, the whole model (including the air chamber) reproduced the prototype at the Froude scale. More precisely, in the absence of incident waves, the volume of air in the model chamber was equal to  $\lambda^3$  times the volume of air in the prototype chamber. In another set of experiments, the air volume was increased by connecting the model air chamber to a rigid-walled reservoir to better approximate the spring-like compressibility effects that occur in the prototype. In this second case, the total volume of air in the model (air chamber, additional reservoir and connecting hoses) was scaled down by a factor equal to  $\lambda^2 \rho_{w,F}/\rho_{w,M}$ , where  $\rho_{w,M}$  and  $\rho_{w,F}$  are the water density in the tank and seawater density, respectively, as explained in Section 2. The model was slack-moored by four mooring lines, as described in detail in Ref. [24].

In all experiments, the top of the air chamber was connected to the fixed additional air reservoir by four parallel flexible hoses. The vertical-axis cylindrical reservoir had thick acrylic rigid walls of 5 mm to guarantee that the volume did not change with the inner pressure oscillations. Manufacturers' information indicated a tensile modulus of 3.2 GPa (ISO 527), a tensile strength of 70 MPa (ISO 527), and a curvature of 120 MPa (ISO 178). The maximum pressure levels in the



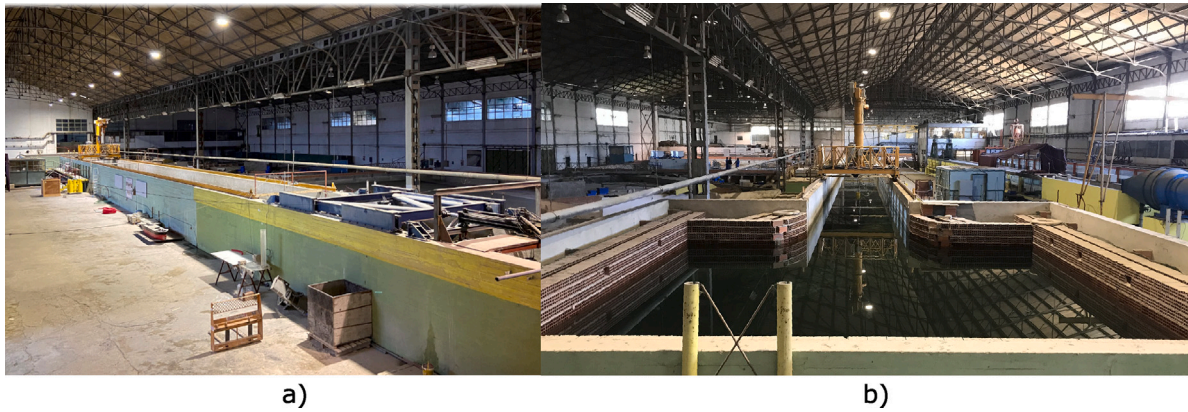


**Fig. 2.** Wave tank COI2 of National Civil Engineering Laboratory (LNEC), Lisbon. (a) External view of the wave flume from the wave generation system perspective (closest elements) to the dissipation basin in the furthest upper part of the photograph. (b) External view of the tank from the passive wave dissipation basin, from this photograph the elongated ‘T’ shape is clearer.

experiments reported here were in the order of  $10^{-3}$  MPa, for which the tank deformation is negligible.

The presence of the four hoses significantly constrained the CD-OWC converter motion. For this reason, all experiments were performed with the hoses in place to ensure similar conditions in both sets of experiments (different air volumes). Valves were placed between the hoses and the extra reservoir to shift the experimental setting between incompressible and compressible modes.

In the experiments reported here, the orifice option to emulate the PTO was adopted, and it represents a self-rectifying air turbine of impulse type, more precisely, a biradial turbine. The dimensionless curves of the turbine used in this work are presented in Ref. [16]. This is a highly efficient self-rectifying air turbine for OWC applications that has exhibited a peak efficiency of 70% under steady-state conditions and an average efficiency of 56% for the control laws tested, having room for improvements regarding control strategies [22].

The tank tests reported here were performed for regular and irregular waves, and three different power take-off (PTO) damping conditions realised through three orifices of 0.01 m, 0.02 m, and 0.03 m diameter, which represent orifice area to air chamber cross-section area ratios of 0.24%, 0.95%, and 2.14%, respectively. Furthermore, the full-scale biradial air turbine equivalent rotor diameters are 0.96 m, 1.97 m, and 2.93 m, respectively. Appendix B presents the equivalency estimation procedure between the biradial air turbine and the orifices used in this work to emulate the PTOs. These diameters were considered based on the research group's experience in designing biradial air turbines for OWCs of equivalent full-scale sizes, and the desired conditions in terms of damping on the air chamber to cover cases with considerable compressibility effect (smallest orifice), as well as optimum and near optimum damping for the CD-OWC and the sea states of Leixões, Portugal.

Regular waves tests comprised two wave heights ( $H = 0.05$  m and  $H = 0.10$  m at model-scale) and various frequencies ranging from 0.45 Hz to 0.65 Hz. Irregular waves comprised one significant wave height,  $H_s = 0.05$  m, and peak frequencies between 0.50 Hz and 0.60 Hz. All tests were performed for both configurations, i.e., using Froude scaling and compressibility scaling of the air chamber.

The wave frequency range was selected on: i) the range of frequencies representative for the response of the device in terms of CWR (see Ref. [24]); ii) the limitations of the wave flume in terms of frequencies possible; and iii) the wave resource on the location for which the geometrical design of the OWC system was optimised hydrodynamically (western coast of Portugal, off Leixões, with a representative peak period of about 11 s).

### 3.2. Wave tank

The experiments were performed at Wave Flume No. 2 (COI2) of the Maritime Hydraulics Department (PHM) of the National Laboratory for Civil Engineering (LNEC), Lisbon, Portugal, see Fig. 2. The wave flume has been in service since 1985. Its dimensions are: total length 82.65 m, width 3.0 m, and height 3.0 m. The tank plan-form is shaped like an elongated ‘T’ at its end, with 11.5 m wide and 11 m long, which serves as a passive dissipation basin. Regular and irregular waves can be generated. The water depth was set at 2.0 m during the experiments reported here. Fig. 3 shows a representation of the experimental setup used in this work.

Wave probes WP1 to WP7 were used to record water surface elevations along the wave flume. Some of the probes were used for the estimation of the reflection coefficients. The reflection analysis was based on the methods presented by [35,36] for two and three-wave probes' measurements by using the software SAM (*Simulação da Agitação Marítima*), developed by LNEC and used in many of the physical testing projects involving their wave tanks.

### 3.3. Instruments

The wave elevation and the position of the OWC in the model were measured with resistive wave probes. These measurements served to compute the incident wave energy and the instantaneous air chamber volume variation. The wave probes had a working range of 0.40 m (accuracy 0.21% Full Scale Span (FSS)).

The air chamber pressure was measured through two different operating range differential pressure sensors: one with a working interval of  $\pm 100$  Pa (accuracy 0.25% FSS), and another with an interval of  $\pm 1250$  Pa (accuracy 0.25% FSS). The pressure was measured at all times in the model air chamber and in the additional tank.

The mooring line forces were measured through submersible load cells. The range of measurements was  $\pm 50$  N with an output voltage range  $\pm 8$  V (accuracy 0.15% FSS). Finally, the movements of the floating CD-OWC were recorded through a six-degree-of-freedom (6-DoF) motion tracking system composed of three infrared cameras. The analog signals of all instruments were acquired using a National Instruments board NI PCIe-6323 with connectors CB-68LP. The sampling rate was 120 Hz.

The orifices were calibrated in experiments with a restrained displacements version of the CD-OWC at 1:40th-scale. The orifice volumetric flow rate was defined by

$$q_{or} = \text{sign}(p) C_d A_{or} \sqrt{2 \frac{|p|}{\rho_a}} \quad (8)$$

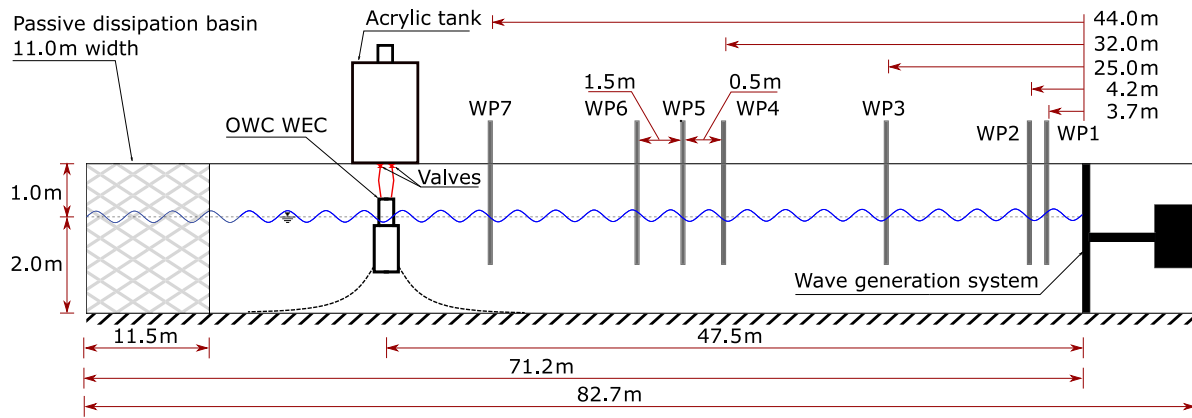


Fig. 3. Cross-section view of experimental setting representation (not at scale) at LNEC COI2 wave tank used in experiments with indication of wave probes positions, OWC WEC location, and tank characteristics.

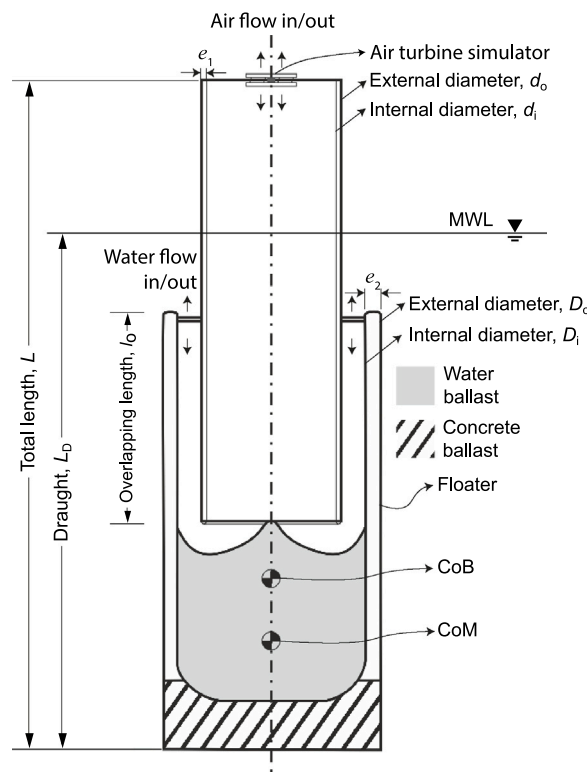


Fig. 4. Main characteristics of the CD-OWC.

where  $q_{or}$  is the volume airflow rate,  $p$  is the measured pressure drop,  $\text{sign}(p)$  represents the sign of  $p$ ,  $\rho_a$  is the air density assumed as  $1.225 \text{ kg/m}^3$ ,  $A_{or}$  is the orifice area, and  $C_d$  is the orifice discharge coefficient. Values of  $C_d$  equal to 0.680, 0.692, and 0.661 were obtained experimentally for orifices of diameter 0.03 m, 0.02 m, and 0.01 m, respectively. Experiments for the determination of the discharged coefficients per orifice comprised a fixed version of the CD-OWC physical model at the same scale (1:40) using Froude scaling, i.e. incompressibility conditions within the air chamber. The experimental runs were performed for a wave height of 0.02 m and wave frequencies of 0.500 Hz, 0.525 Hz, 0.500 Hz, 0.575 Hz, 0.600 Hz, and 0.650 Hz.  $C_d$  values presented represent the average of at least 20 different measurements per orifice under regular waves. Differences between measurements were found to be less than 4%. The procedure used is equivalent to the one presented in [37].

### 3.4. CD-OWC full scale design and physical model

The main characteristics of the full-scale CD-OWC floater and the 1:40-scale model are shown in Fig. 4. The full-scale design resulted from an optimisation process based on the wave climate of the western coast of Portugal, as presented in Ref. [38]. The corresponding prototype and model values are presented in Table 1. The table also gives the two volumes of the air chamber used in the tank tests. One corresponds to the volume in Froude mode and the other to the compressibility mode. Fig. 5 shows a CAD representation of the model and a photograph of the model standing on a precision scale.

Fig. 6 shows the experimental setup with the additional air chamber (acrylic tank), connected with the floating CD-OWC model (at the bottom) through four large-diameter flexible hoses (in red). The system used four mooring lines, such as the ones described in Ref. [24].

**Table 1**

Dimensions of the full-scale prototype and the 1:40-scale model of the CD-OWC. See Fig. 4 for the meaning of the symbols.

Parameter	Full-scale	1:40-scale model
$L$ [m]	43.0	1.075
$L_D$ [m]	33.0	0.825
$l_o$ [m]	13.0	0.325
$D_o$ [m]	14.0	0.350
$D_i$ [m]	12.0	0.300
$d_o$ [m]	9.2	0.230
$d_i$ [m]	8.2	0.205
$e_1$ [m]	0.5	0.0125
$e_2$ [m]	1.1	0.0250
$M$ [kg]	$1.818 \times 10^6$	28.4
$I$ [kg m <sup>2</sup> ]	$288.1 \times 10^6$	2.8
CoB to MWL [m]	22.6	0.565
CoM to MWL [m]	26.3	0.657
Air chamber volume $V$ (Froude) [m <sup>3</sup> ]	528.1	$8.251 \times 10^{-3}$
Air chamber volume $V$ (Compressibility) [m <sup>3</sup> ]	528.1	0.330



Fig. 5. CAD representation of the model (left) and a photograph of the model standing on a scale (right).

## 4. Experimental results

This section presents the major findings and their discussion. Natural frequencies, capture width ratio, internal water column displacement, buoy motions, pressure in the air chamber are presented. In addition, inhalation and exhalation processes based on experimental data and a new compressibility factor are discussed.

In all experiments, repeats were performed in different numbers, proportions, and days to grasp the possible errors. In general, a good agreement among measurements was found. All values presented in this paper represent average values for the same conditions' tests, and the uncertainty ranges with a confidence interval of 95% are shown.

### 4.1. Natural frequencies

Table 2 shows the mean values of the natural frequencies  $f_n$  obtained experimentally, based on the average of at least three tests per degree of freedom for the CD-OWC model under the experimental configuration. The decay tests showed good repeatability, despite the inherent difficulties in perturbing the device only along one axis at a time, especially in heave.

Although the device is axisymmetric, there are some differences between the natural frequencies of surge and sway, and roll and pitch, which are probably due partly to small differences in the damping

impose by the connections to the acrylic tank. The natural frequency of the internal mass of water (water column),  $\omega_{n_{\text{heave},2}}$ , was estimated theoretically to be about 0.526 Hz for the CD-OWC at the model scale, from (see Ref. [39], Eq. (5.324)),

$$\omega_{n_{\text{heave},2}} = \sqrt{\frac{\rho_w g S_{\text{OWC}}}{m_2 + A_{99}(\omega_{n_{\text{heave},2}})}}, \quad (9)$$

where,  $A_{99}(\omega_{n_{\text{heave},2}})$  represents the added mass of the internal mass of water in heave at  $\omega_{n_{\text{heave},2}}$ , which requires an iterative approach. The added mass was computed using the three-dimensional panel method software WAMIT© version 7. The definition of the system's geometry in WAMIT© assumed the internal free surface of the OWC as a weightless rigid piston of mass  $m_2$ .

### 4.2. Regular waves

Tests were performed for wave heights of 0.05 m and wave frequencies from 0.450 Hz up to 0.650 Hz, no constant frequency steps were used, giving more resolution around expected peaks, and selection was also made considering time constraints available for the wave tank. Furthermore, tests were performed for a wave height of 0.10 m, and wave frequencies from 0.500 Hz up to 0.600 Hz, with a frequency step of 0.025 Hz. The frequency range for the highest wave height was narrower to avoid physical model's upper lit failure. Tests were done

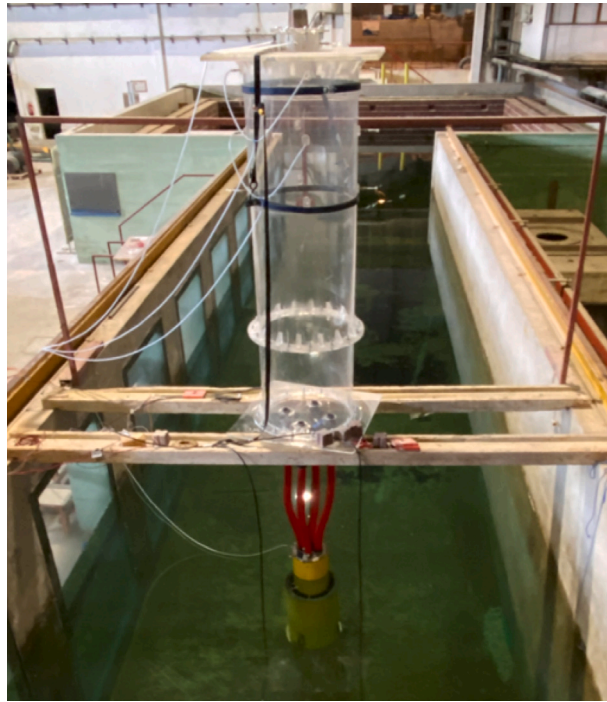


Fig. 6. Experimental set-up. From top to bottom: the additional acrylic air-reservoir, four flexible tubes (in red) connected in parallel to the floating converter.

Table 2

Experimental natural frequencies  $f_n$  for the 6-DoF obtained through decay tests of a CD-OWC and an orifice diameter of 0.03 m.

	Surge	Sway	Heave	Roll	Pitch	Yaw
$f_n$ [Hz]	0.125	0.102	0.743	0.668	0.614	1.590

for both configurations (Froude and compressibility modes) and three different orifice diameters of 0.01 m, 0.02 m, and 0.03 m. The pressure was measured at all times in both the acrylic tank and the CD-OWC model chamber. This helps monitor any leakages and confirm that flow losses are negligible in the valves and fittings in the compressibility mode.

#### 4.2.1. Capture width ratio

The capture width ratio (CWR) is the dimensionless ratio between the time-averaged pneumatic power ( $\bar{P}$ ) and the time-averaged wave power per unit crest length ( $\bar{P}_w$ ) multiplied by the characteristic length of the device ( $D$ ), as follows,

$$\text{CWR} = \frac{\bar{P}}{D \bar{P}_w}, \quad (10)$$

$\bar{P}$  is obtained from averaging the instantaneous power  $P$  over the useful test time interval, with  $P$  being expressed as

$$P = p q_{or}. \quad (11)$$

The volumetric airflow rate ( $q_{or}$ ) is estimated by using Eq. (8). For regular waves, the time-averaged incident wave power per unit crest length is computed as

$$\bar{P}_w = \frac{1}{2} \rho_w g \bar{A}_w^2 c_g, \quad (12)$$

where  $\rho_w$  is the density of water,  $\bar{A}_w$  is the time-averaged measured wave amplitude ( $A_w = H/2$ ), and  $c_g$  is the group velocity [40]. The diameter of the outer duct  $D_o = 0.35$  m was considered the characteristic length of the device to define the capture width ratio of the CD-OWC.

Fig. 7(a) shows the capture width ratio for both compressible cases (compressibility mode) and incompressible cases (Froude mode), and the three orifices used under regular waves with height  $H = 0.05$  m.

Hereinafter, vertical bars in the figures represent the uncertainty range in the measurements for a confidence interval of 95%. It can be observed that the highest CWR is achieved for both compressible and incompressible cases with an orifice of 0.02 m diameter.

Regarding the effects of the extra volume added to the air chamber, it is in general observed that for the orifice of 0.02 m diameter, all incompressible cases show higher CWR than the compressible ones. The differences between the compressible and the incompressible cases are mostly within a range of 10% and 18%, with these differences increasing with decreasing frequencies starting at around 0.510 Hz (up to 37%).

The highest differences between compressible and incompressible CWR are noted for the orifice of 0.01 m diameter. For all frequencies, the compressible case presents CWR higher than values obtained in Froude mode.

The performance of the device with the orifice of 0.02 m is the best among the three orifices as aforementioned. For  $H = 0.05$  m, the maximum CWR is about 0.40 at a frequency of 0.575 Hz. It is observed in general four regions of high CWR. The first region is between 0.500 Hz and 0.530 Hz, believed to be associated with the natural frequency of the internal OWC. Region that for the 0.02 m orifice is more diffuse than for the other orifices, with a maximum CWR of around 0.32, associated probably to the more favourable damping at those frequencies. Afterwards, it is observed a second region with a better-defined peak at about 0.550 Hz and a third region with a very notorious peak at a frequency of 0.575 Hz in which the highest CWR occurs. The latter peaks are most probably associated with the coupling between pitch-surge, roll-sway, and their effects on the internal OWC (as it is probably the case of a sloshing induced by the surge mode on the OWC at about 0.550 Hz, as described in Section 4.4, and that was not expected *a priori*). Buoy's motions are also presented in the next



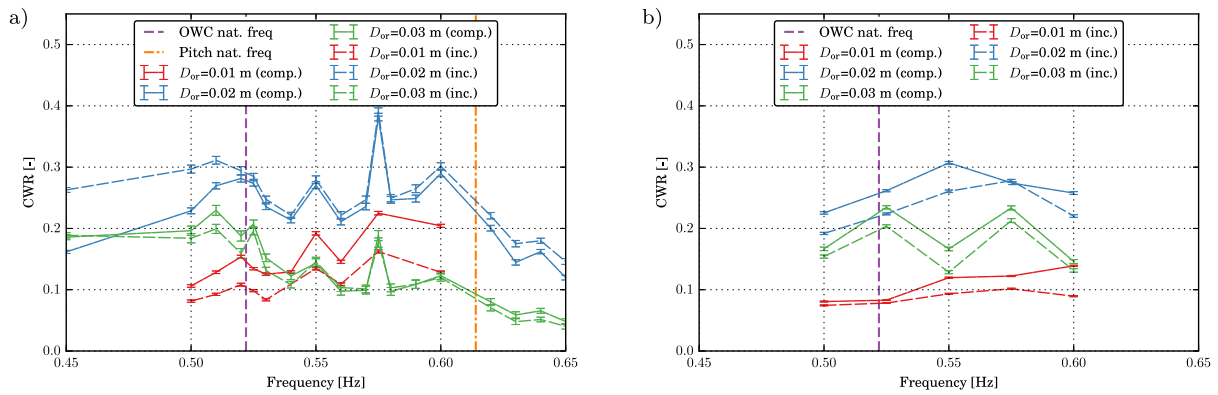


Fig. 7. CWR versus wave frequency for both the compressible (comp.) and incompressible (inc.) cases and orifice diameters  $D_{or} = 0.01, 0.02$  and  $0.03$  m. Regular waves tests for (a)  $H = 0.05$  m and (b)  $H = 0.10$  m.

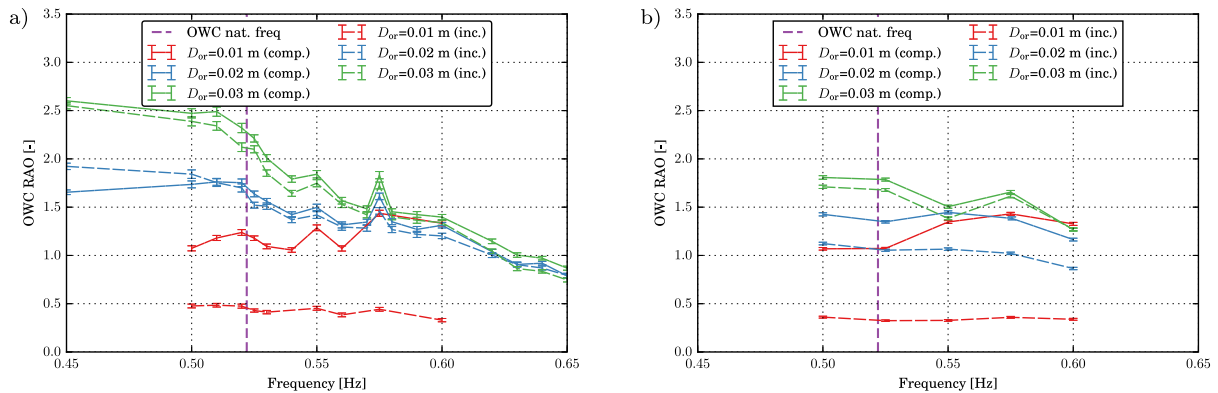


Fig. 8. Internal OWC elevation response amplitude operator (OWC RAO) versus wave frequencies for both compressible (comp.) and incompressible (inc.) cases for regular waves with (a)  $H = 0.05$  m and (b)  $H = 0.10$  m.

sections. Finally, there is another peak at around  $0.600$  Hz. It is again more pronounced for the  $0.02$  m orifice (up to around  $0.30$ ), and later on, the CWR decreases for values below  $0.20$ . It was observed some slight parametric rolling for wave frequencies between  $0.600$  Hz and  $0.650$  Hz, worsened towards the highest frequency.

For the tests performed with wave height  $H = 0.10$  m (Fig. 7(b)), it is observed that the orifice of  $0.02$  m diameter induces the highest CWR of around  $0.30$  at  $0.550$  Hz, under compressible conditions, with a relative difference of about  $15\%$  compared to the incompressible case. The curve is flatter for this orifice, and the same occurs for the case of a  $0.01$  m diameter orifice. The CWR curve obtained for the  $0.03$  m orifice is less flat than for other orifice diameters, with clear peaks at  $0.518$  Hz and  $0.575$  Hz. Comparing the compressible cases with the incompressible ones, it is obvious that the CWRs for all compressible cases are higher than the corresponding incompressible results. The higher wave height induces a higher spring-like compressibility effect in the air chamber.

The comparison of the three orifices for the two wave heights indicates that the damping induced by the orifices (PTO) influence strongly the CWR, in agreement with other reported works [25,26,29,41]. Refs. [29,41] made comparisons of compressible and incompressible cases using CFD simulations of fixed OWCs under regular waves and only pointed out the negative impacts of air compressibility. They reported reductions of CWR under compressibility conditions up to  $12\%$ . They also highlighted that the larger the physical model scale, the lower the ‘overestimation’ of CWR (for model scales greater than  $1:50$ ). In contrast, Ref. [26] reported experimental results, only in regular waves, indicating that compressibility effects may create positive or negative effects depending on damping and wave conditions; they reported differences in CWR under compressibility conditions of about

$\pm 30\%$ . This is the case also in the results reported in this work for the floating CD-OWC. Although cases with more significant differences have been identified in this work (up to  $55\%$  higher CWR in very compressible tests).

The fact of having both higher and lower CWRs considering compressibility effects when compared to incompressible equivalent cases have been demonstrated theoretically in Ref. [25]. This has practical implications because disregarding the compressibility effects in PTO selection and optimisation may lead to considerable lower system’s performance.

#### 4.2.2. Internal OWC elevation

The elevation of the internal water column is characterised through a dimensionless response amplitude operator defined as  $RAO = \bar{A}_{owc} / \bar{A}_w$ , where  $\bar{A}_{owc}$  represents the mean amplitude of the internal mass of water (OWC), and  $\bar{A}_w$  the mean amplitude of the waves. The mean amplitudes  $\bar{A}_{owc}$  and  $\bar{A}_w$  were computed as  $\bar{A} = \sqrt{2} \|\mathbf{A}\|$ , where  $\mathbf{A}$  is the vector of the amplitudes obtained by a Fast Fourier Transform of the water elevation.

Fig. 8(a) shows the OWC RAOs under regular waves of height  $H = 0.05$  m for compressible and incompressible cases and the three chosen orifices. In general, it can be observed that the OWC RAOs are higher for larger orifice diameters, i.e., in the way that the PTO damping decreases, the OWC displaces with lesser restrictions. This was obviously expected.

The differences in OWC RAOs between the compressible and incompressible cases are notoriously higher for the orifice of  $0.01$  m, which is more accentuated for the higher wave height. Results of OWC RAOs for a wave height of  $0.10$  m are shown in Fig. 8(b). In this case, the OWC RAOs for the compressible cases are always higher than the ones



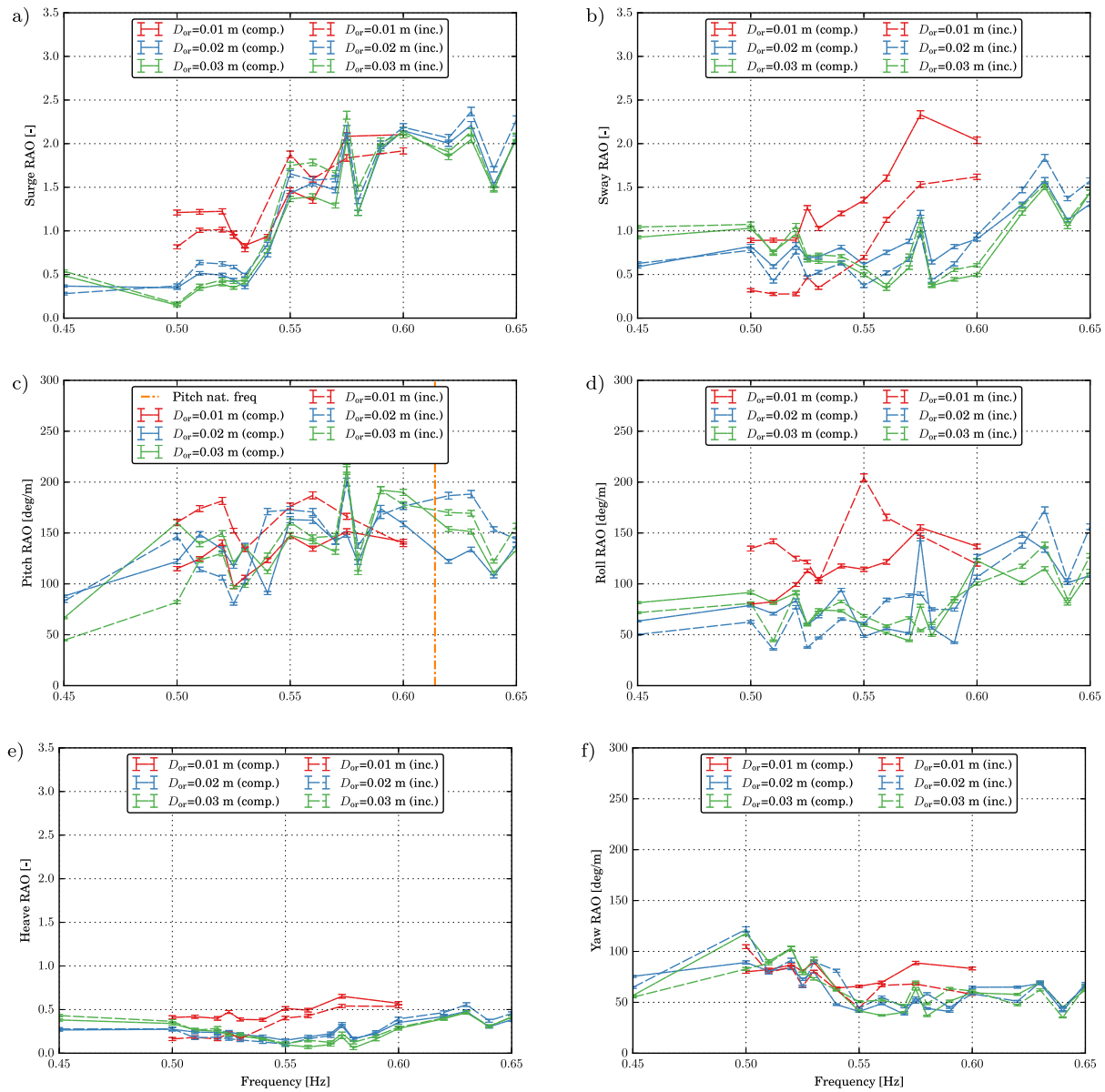


Fig. 9. Motion response amplitude operators of the CD-OWC for 6-DoF under regular waves with  $H = 0.05$  m and various wave frequencies. Data is shown at model scale.

under incompressible conditions. The RAOs differences get higher when the orifice diameter decreases, where the higher damping induces a significant compressibility effect on the system.

Refs. [29,41] report the effect of compressibility on the internal OWC displacement based on CFD numerical results. They observed only minor differences in the relative difference of the OWC RAOs between compressible and incompressible cases. Nevertheless, Simonetti et al. (2018) [41] realised that higher pressure within the air chamber would increase differences. This is the case for the CD-OWC.

#### 4.2.3. Device motion

Fig. 9 presents the RAOs of the CD-OWC under regular waves with  $H = 0.05$  m for compressible and incompressible cases. It can be observed that after 0.600 Hz, the amplitudes in the surge, pitch, sway, and roll increase due to probably the natural frequencies of pitch and roll. There seems to be a coupling between pitch and the heave motion of the internal OWC. Pitch motions seem to increase also towards the natural frequency estimated for the OWC (0.526 Hz). The connections to the tank creates strong constraints in the heave motions of the CD-OWC, showing a relatively flat curve. Furthermore, it is also evident

that the air chamber damping imposed by the orifices also affects the device's motions, especially for  $D_{or} = 0.01$  m.

When the incident wave height is larger, the influence of the air chamber damping and the compressibility effect turn more evident, see Fig. 10. The differences between the motions, practically in all modes, are considerably different in magnitude between the compressible and incompressible cases for  $D_{or} = 0.01$  m. Almost in all modes of movement, the compressible cases present larger amplitudes.

#### 4.2.4. Pressure oscillations

The pressure oscillations were analysed in the frequency domain, and the mean pressure amplitude  $\bar{p}$  was computed as done for the mean wave amplitude (see Section 4.2.2). The dimensionless pressure spectral amplitude  $\hat{p}$  is computed as

$$\hat{p} = \frac{\bar{p}}{\rho_w g \bar{A}_w} \quad (13)$$

Fig. 11(a) shows both compressible and incompressible cases' results for the three orifice diameters and a wave height  $H = 0.05$  m. It can be observed that for orifices of 0.02 m and 0.03 m diameter,

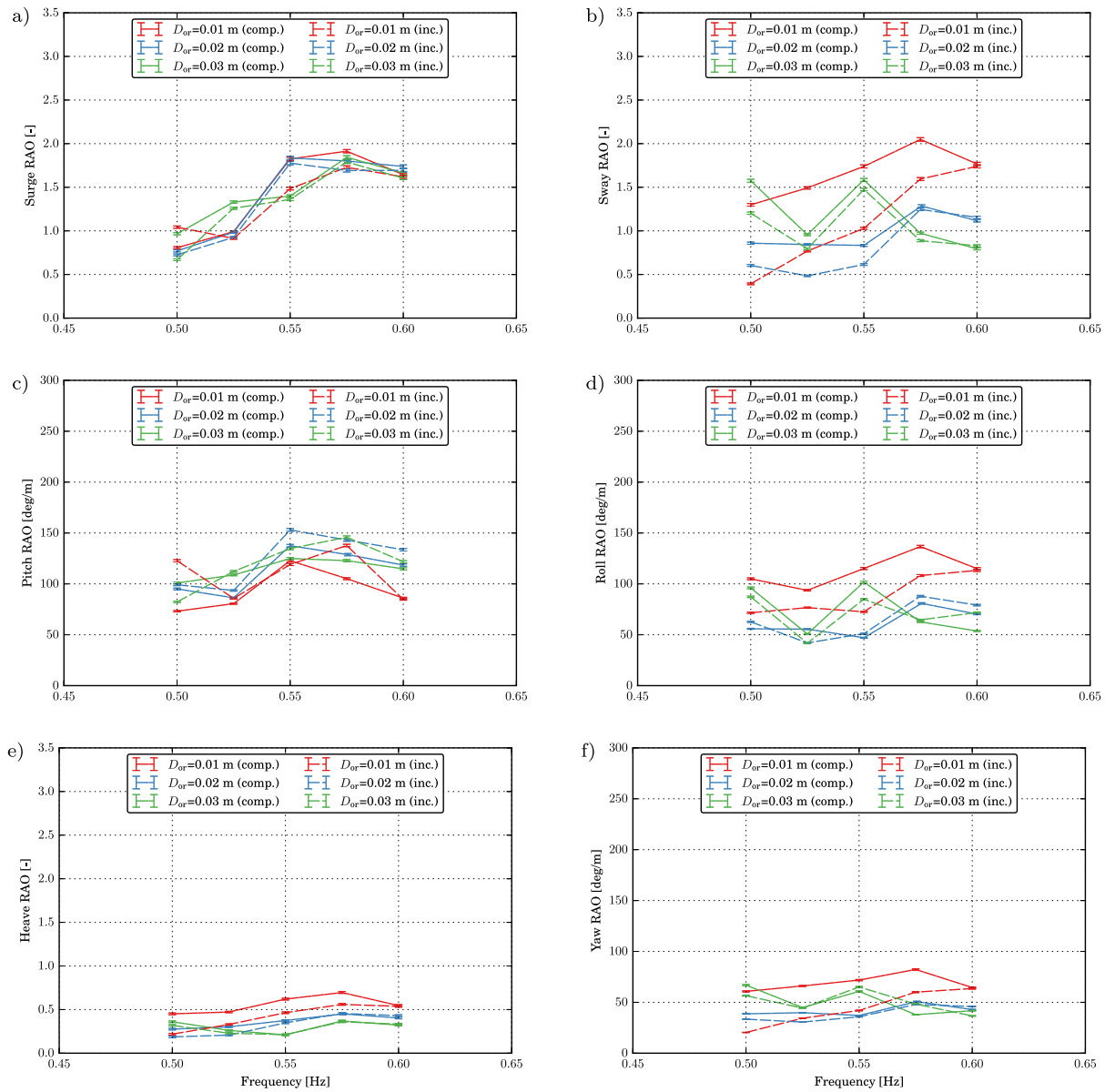


Fig. 10. As in Fig. 9 for  $H = 0.10$  m.

the dimensionless pressure amplitude for both compressible and incompressible cases are very similar. An exception is for frequencies 0.450 Hz, 0.500 Hz, and 0.510 Hz, and the 0.02 m diameter orifice, in which the incompressible case showed higher pressure amplitudes. The differences increase with decreasing frequency.

In contrast, it can be seen that for the 0.01 m orifice diameter, the dimensionless pressure amplitude is considerably higher for the compressible case in comparison to the incompressible one. The highest difference (about 25%) is observed at 0.600 Hz. When the pressure level increases, the relative differences of the pressure amplitudes increase between the compressible and incompressible cases for a wave height  $H = 0.05$  m.

The regular wave tests with  $H = 0.10$  m show higher dimensionless pressure amplitudes for the compressible cases than the incompressible ones, Fig. 11(b). Most pronounced relative pressure amplitude differences occur for the highest damping. Maximum differences are around 20%, 10%, and 12% for 0.01 m, 0.02 m, and 0.03 m orifice diameters, respectively. The dimensional pressure levels are much higher for  $H = 0.10$  m wave height than  $H = 0.05$  m. It is evident that the higher the damping, the higher the effect on the pressure within the air chamber, but this effect is not directly related to the system's performance.

#### 4.3. Irregular waves

The irregular wave test results presented in this section considered a significant wave height  $H_s = 0.05$  m and five selected peak frequencies: 0.500 Hz, 0.525 Hz, 0.550 Hz, 0.575 Hz, and 0.600 Hz, for orifices with  $D_{or} = 0.02$  m and  $D_{or} = 0.03$  m. These two orifices were selected because they are closer to the optimal damping for the tested model. Tests considered incompressibility and compressibility effects under irregular waves using Pierson–Moskowitz spectra.

##### 4.3.1. Capture width ratio

The CWRs for irregular waves with significant wave height  $H_s = 0.05$  m and two orifice diameters (0.02 m and 0.03 m) are shown in Fig. 12(a). It is observed that for both orifices, the compressible CWRs are higher than the incompressible ones. Higher capture widths were recorded at around 0.518 Hz. Nevertheless, the CWR variation of each case is not as pronounced as in regular waves.

As expected, CWRs were considerably reduced for irregular waves, and present somewhat flatter curves for both compressible and incompressible cases. Interestingly, the compressible cases present better

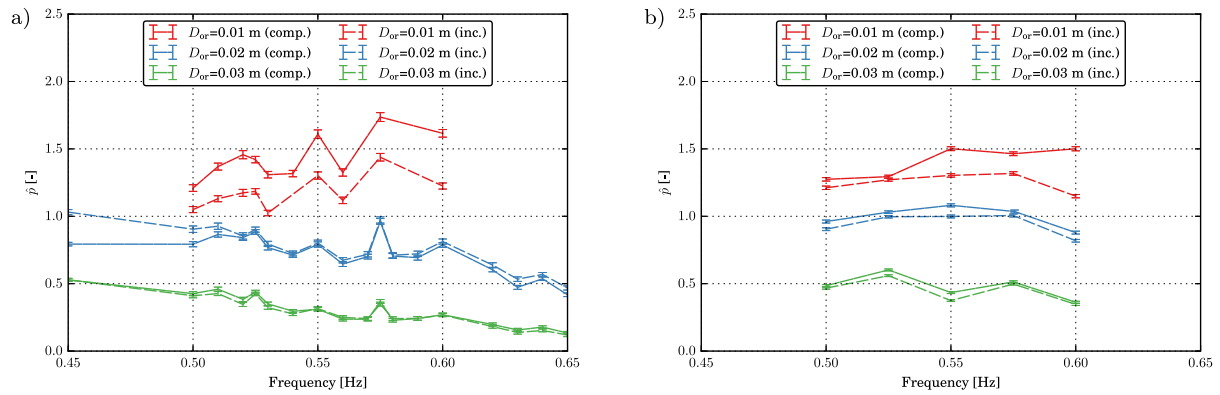


Fig. 11. (a) Air chamber dimensionless pressure spectral amplitude  $\hat{p}$  versus wave frequencies for both compressible (comp.) and incompressible (inc.) cases for regular waves with (a)  $H = 0.05$  m and (b)  $H = 0.10$  m.

performance than the incompressible ones for any point tested. Nevertheless, it should be highlighted that the relative differences among cases were about 12%. In Ref. [42], a numerical study showed that disregarding the air compressibility effects on a fixed OWC model results in a relative error of the mean annual conversion efficiency of about 10.6%. The referred study considered 73 irregular sea-states and highlighted the more complex behaviour in floating OWCs due to the hydrodynamic and aerodynamic coupling, which affects the floating body dynamics.

#### 4.3.2. Internal OWC elevation

Under irregular wave conditions, the internal OWC elevation is similar to regular waves, see Fig. 12(b). Compressible RAOs are higher in all cases for the two orifices tested, and the relative differences between the compressible RAOs and the incompressible RAOs do not vary considerably. The maximum relative differences were found to be around 14% and 10% for the 0.02 m and 0.03 m orifice diameter, respectively.

#### 4.3.3. Pressure oscillations

Relative differences do not exceed 7% between the compressible and incompressible cases, see Fig. 12(c). The relative differences between the compressible and incompressible cases are smaller for irregular waves than for regular waves. Complementary, it is observed that the compressible cases' differential amplitudes are generally slightly higher than the corresponding incompressible cases. Nevertheless, the differences are minimal and mostly within the uncertainty interval of measurements.

#### 4.4. Analysis of selected time series

An interval of a time series was analysed in more detail. One regular-wave case with  $H = 0.05$  m and  $f = 0.550$  Hz is selected. Figs. 13(a) to (c) show the dimensionless elevation of the internal OWC,  $\hat{z} = z_{OWC}/\bar{A}_w$ , and pressure,  $\hat{p}$  (see Eq. (13)), for the compressible and incompressible cases and the three orifices studied. For the 0.01 m orifice diameter, both OWC elevation and pressure amplitudes are higher for the compressible case. Furthermore, it is shown that the inhalation and exhalation cycles are not symmetric in both compressible and incompressible cases (see Ref. [25] for a discussion on the topic).

An interesting observation is that the OWC elevation for the incompressible case presents a very disturbed water-free surface inside the chamber for 0.550 Hz. This may be probably associated with some internal sloshing of the inner mass of water, due to the proximity of the sloshing natural frequency for surge and the wave frequency of 0.550 Hz, as discussed further at the end of this section. Nevertheless,

other reasons may be associated with transverse waves in the tank that were not observed during the tests for wave frequency of 0.550 Hz, and also may be due to some coupled effects related to the restrained motion of the device either because of moorings and/or the connecting hoses and added acrylic tank. Results of CWR and OWC inner surface elevation for this specific frequency should be looked with care, due to increased uncertainties and the fact that only one wave probe was used to measure the inner surface elevation.

It can be observed also the phase shift of the pressure oscillation to the OWC elevation when comparing the compressible and incompressible cases, which is an expected result of the spring-like effect variation of the air in the chamber. The difference in phase shift between the pressure and the volumetric airflow, the latter related to the OWC elevation, is associated with the amount of reactive power in the system. The reader is referred to Ref. [25] for a more detailed discussion on reactive power in OWCs. Furthermore, in the compressible case, the phase difference between the pressure oscillation and the OWC elevation is less than for the incompressible one. In this case, the CWR for the compressible case is about 30% higher than for the incompressible case.

The 0.02 m orifice diameter case represents the best performance case in terms of CWR among all orifices tested. In Fig. 13(b), it is observed that the OWC displacement amplitude and pressure oscillation are slightly higher in the compressible configuration than in the incompressible one. When comparing compressible and incompressible cases, a phase shift of the pressure oscillation to the OWC elevation is evident. The relative difference in CWR between both cases is only about 3%.

Fig. 13(c) presents the time series for the 0.03 m orifice diameter. It is observed that both pressure oscillation and OWC elevation have partially the same amplitude and phases for both cases. The CWR is practically the same (relative difference of 1.4%).

Figs. 14(a) and (b) show the dimensionless OWC velocity and pressure time series for orifice diameters (a) 0.01 m and (b) 0.02 m,  $H = 0.05$  m, and  $f = 0.550$  Hz for both compressible and incompressible cases. The comparison between these two figures demonstrates that the power output is higher when the time derivative of the relative OWC elevation (OWC velocity) is in phase with the pressure, see Fig. 14(b). The higher CWR is obtained with the 0.02 m orifice diameter, where the phases between the OWC velocity and pressure are closer to each other. This indicates that there is less reactive power under these conditions within the air chamber (see Ref. [25]).

High-frequency components can be identified in the OWC velocities  $\dot{\hat{z}}$  depicted in Figs. 14(a) and (b). A Fast Fourier transform of the CD-OWC's displacements, the relative pressure  $\hat{p}$  and OWC velocity  $\dot{\hat{z}}$  is shown in Fig. 15 for the 0.01 m orifice diameter case and wave

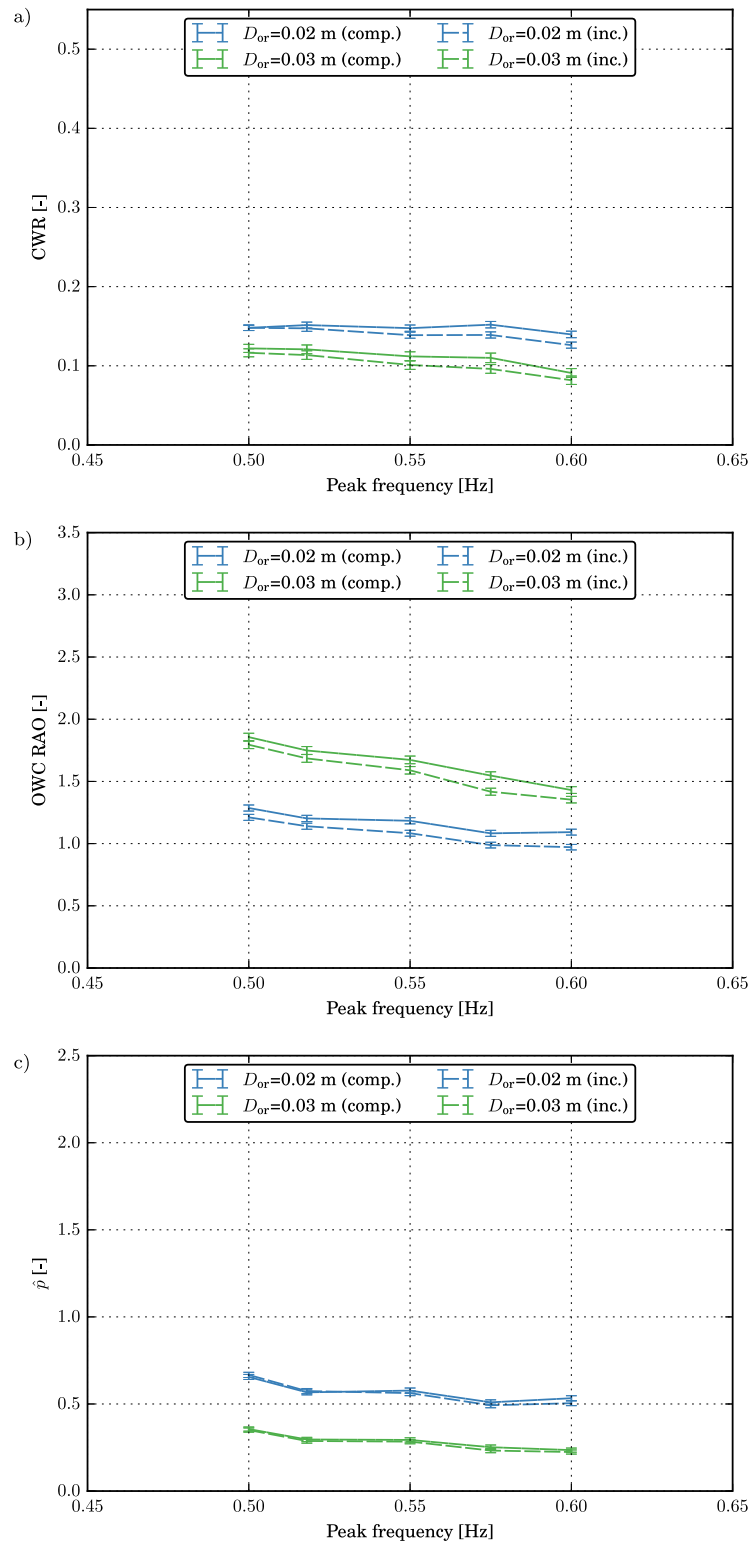


**Fig. 12.** (a) CWR, (b) internal OWC RAO, and (c) air chamber dimensionless pressure spectral amplitude  $\hat{p}$  versus peak frequency for both compressible (comp.) and incompressible (inc.) cases with a significant wave height of  $H_s = 0.05$  m.

frequency  $f = 0.550$  Hz. The FFT of the OWC velocity reveals that the high-frequency component may be related to the 4th harmonic of wave frequency, i.e.,  $f = 4 \times 0.550 = 2.200$  Hz. This high frequency appearing in the OWC velocity is probably due to sloshing mode (1,1) induced in the OWC free surface by the surge motion (the motion with the highest

horizontal amplitude). The sloshing mode (1,1) has a natural frequency of  $f_{11}^{\text{slosh}} = 2.112$  Hz, see [43]. This frequency is very close to the 4th harmonic shown in Fig. 15. The high frequency associated with sloshing is not found in the pressure signal. The same effect is observed on the other OWC displacement velocities depicted in Figs. 14(a) and (b).



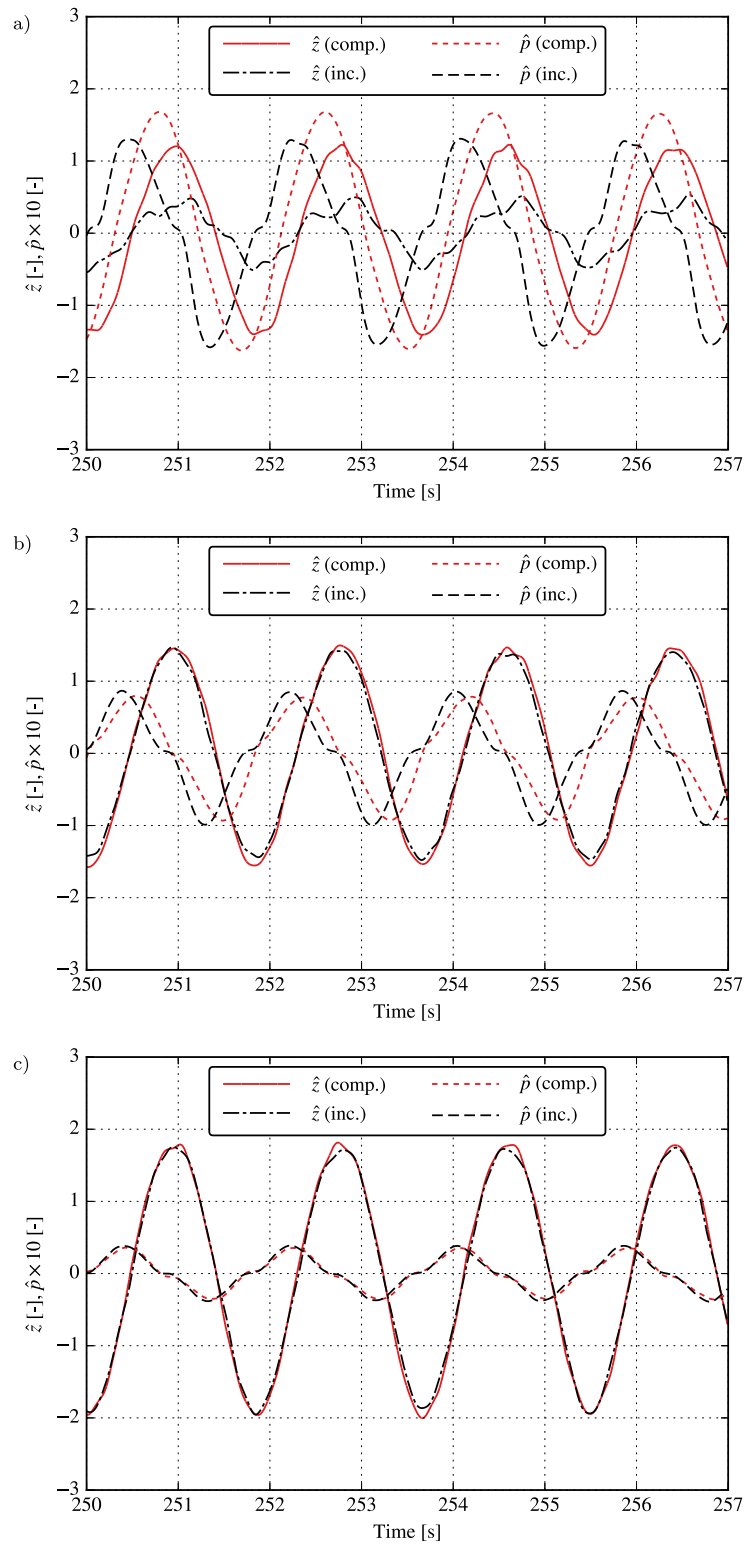


**Fig. 13.** Dimensionless OWC elevation  $\hat{z}$  and pressure oscillation  $\hat{p}$  time series in the air chamber for  $H = 0.05$  m, and  $f = 0.550$  Hz for both compressible (comp.) and incompressible (inc.) cases. Plots for (a)  $D_{or} = 0.01$  m; (b)  $D_{or} = 0.02$  m, and (c)  $D_{or} = 0.03$  m.

#### 4.5. Inhalation and exhalation processes

More detailed information about the inhalation and exhalation cycles regarding the relative power difference produced is presented in Fig. 16 for compressible and incompressible cases and the three orifices considering a selected range of frequencies. The figure shows the ratio

between the mean power output during all inhalation cycles per case and the corresponding value during exhalation.

Values above 1 imply a higher mean power output during inhalation cycles, and values below 1 suggest that more power output is obtained in exhalation. It can be seen that for the 0.02 m orifice – the test case with greater CWR – there is more power output during inhalation cycles for frequencies between 0.500 Hz and 0.575 Hz, recording maximum

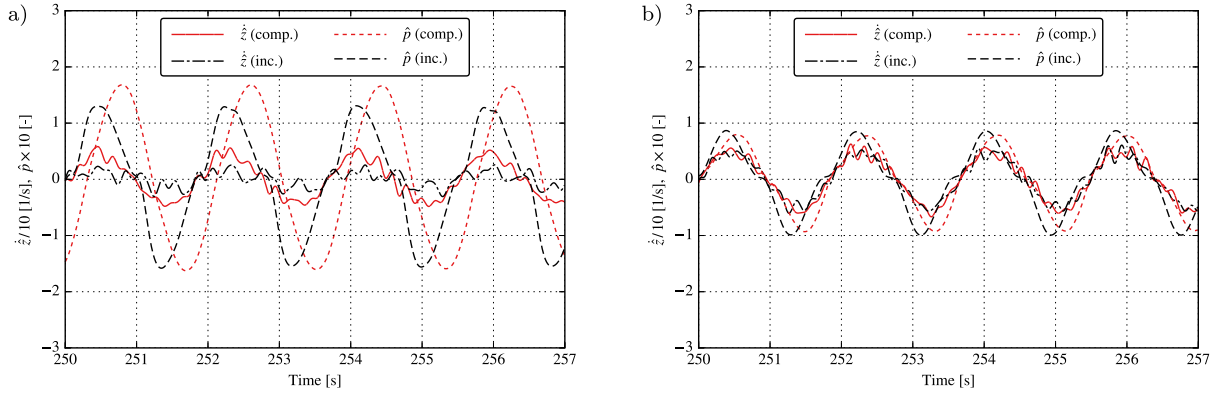


Fig. 14. Dimensionless time-derivative of the OWC elevation  $\dot{z}$  and pressure oscillation  $\dot{p}$  time series in the air chamber for (a)  $D_{or} = 0.01$  m and (b)  $D_{or} = 0.02$  m. Regular waves for  $H = 0.05$  m and  $f = 0.550$  Hz, and compressible (comp.) and incompressible (inc.) cases.

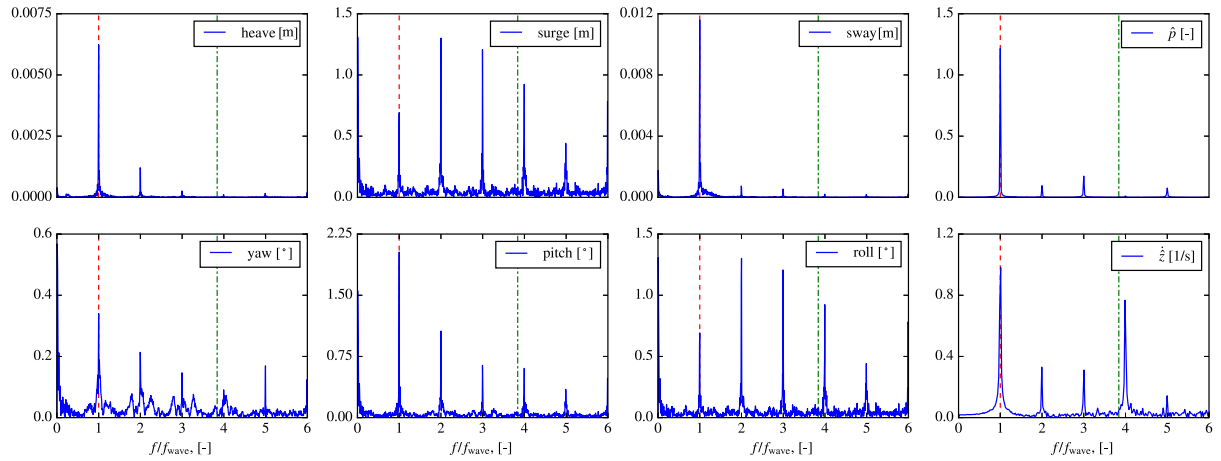


Fig. 15. Fast Fourier transform of CD-OWC's displacements, as well as the relative pressure  $\dot{p}$  and OWC velocity  $\dot{z}$  for orifice diameter 0.01 m and wave frequency  $f_{wave} = 0.550$  Hz under incompressible conditions. The vertical dashed line is wave frequency and the vertical dash-dot line is the sloshing natural frequency for mode (1,1) ( $f_{11}^{slosh} = 2.112$  Hz).

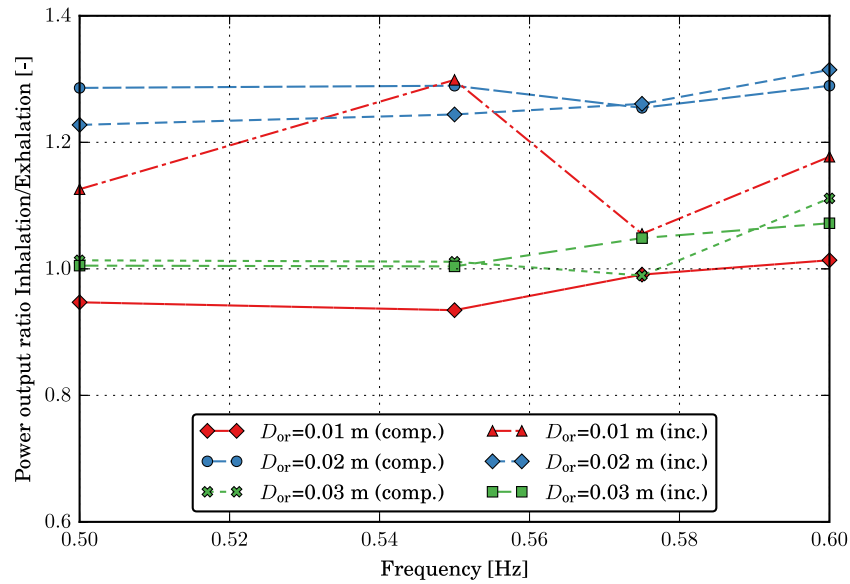


Fig. 16. Power output ratio during the inhalation process over the exhalation process for  $D_{or} = 0.01$  m, 0.02 m and 0.03 m, under regular waves with  $H = 0.05$  m and selected frequencies.

values of around 1.3 (around 30% higher than in exhalation cycles). For the 0.03 m orifice, both cycles have approximately the same power output, with differences more accentuated for higher frequencies. Finally,

the behaviour is different for the smaller orifice (0.01 m diameter), which produces higher stiffness within the chamber. The incompressible case shows higher values (above 1) of the power output ratio for

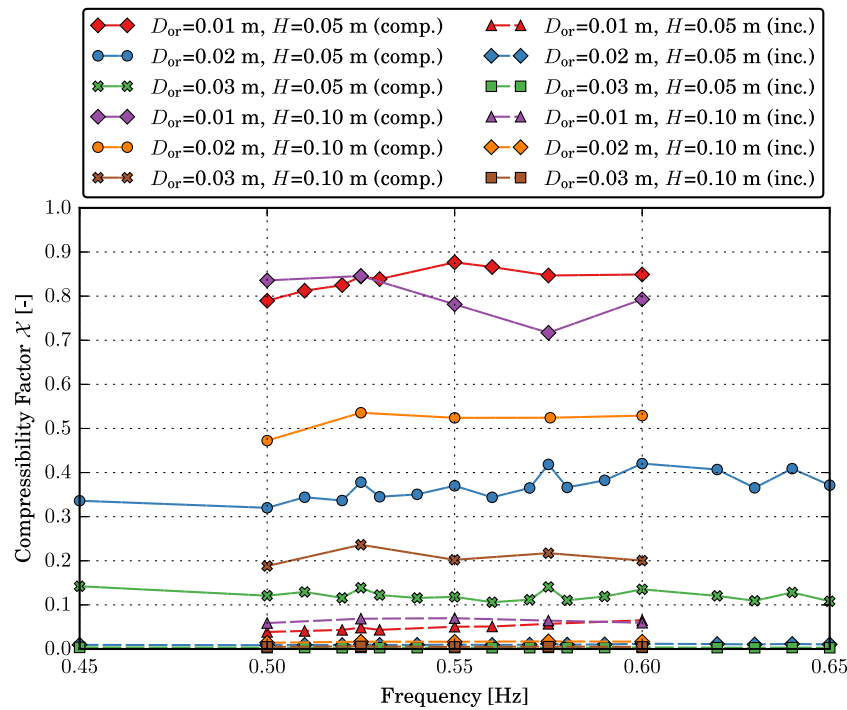


Fig. 17. Compressibility factor versus frequencies for regular wave tests performed under compressible and incompressible conditions.

all frequencies and presents relatively large variations compared to the other orifices. In contrast, there are at least two frequencies (0.500 Hz and 0.550 Hz) for the compressible case where the power ratio is clearly below 1 (around 0.95), while for 0.575 Hz and 0.600 Hz is about 1.

#### 4.6. Compressibility factor for experimental testing comparison

It is worth introducing a dimensionless coefficient that can provide the experimentalists with a quantitative measure of the spring-like compressibility effects on the air chamber in the OWC WEC design. In this sense, a new compressibility factor  $\chi$  is defined as follows (see derivation in Appendix A)

$$\chi = \frac{\mathcal{P}}{k p_{\text{atm}}} \frac{h_{\text{ac}}}{Z_{\text{owc}}}, \quad (14)$$

where  $\mathcal{P}$  is the relative pressure amplitude inside the air chamber,  $p_{\text{atm}}$  is the atmospheric pressure,  $h_{\text{ac}} = V_0/S_{\text{owc}}$  is the equivalent height of the air chamber,  $V_0$  is the air chamber volume in calm water,  $S_{\text{owc}}$  is the area of the OWC at the free surface,  $Z_{\text{owc}}$  is the amplitude of the relative motion between the OWC free surface and the buoy  $z_{\text{owc}} = z_2 - z_1$  (see Fig. 1), and  $k$  is the polytropic exponent ( $k = \gamma$  for an isentropic expansion, where  $\gamma$  is the ratio of specific heats ratio for air).

Values of the compressibility factor  $\chi$  close to zero indicate a stiff air chamber. In contrast, the spring-like compressibility effects are significant when  $\chi$  approaches one. Note that there is no upper limiting value, i.e., the compressibility factor may be greater than one.

Fig. 17 presents the proposed compressibility factor versus wave frequency for all regular tests performed and for both compressible and incompressible cases. For all compressible cases, the factor is above 0.1, and it is possible to grasp the relative influence of the compressibility effects between cases. All compressible cases present values from 0.1 up to around 0.9. The incompressible cases present values lower than 0.1. Comparing the compressibility factor for the 0.01 m orifice diameter tests, factors' values for the compressible cases are much higher. This compressibility factor may be used indicatively to design or to analyse experimental campaigns, using appropriate guesses for the pressure level and the OWC elevation. The latter may be assumed, as a first guess, as the wave amplitude. Complementary, the proposed factor

can also be used to evaluate the equivalent air chamber height  $h_{\text{ac}}$  in OWC systems for which compressibility effects are predominant or important. So, it may also provide comparative insights when designing and simulating OWC wave energy converters.

## 5. Conclusions

Experimental results showed significant effects of air compressibility on the performance of a floating OWC WEC. A coaxial-duct OWC was tested in regular waves at a scale 1:40 in two configurations: one with an air chamber whose volume was Froude scaled, and another one whose total air volume (including a large connected reservoir) was defined by the aero-thermodynamic similarity.

Several key conclusions may be highlighted: (i) compressibility effects can increase or decrease the mean power absorbed by the PTO, depending on wave period, which agrees with the other theoretical findings and the experimental results found in the literature for fixed OWCs; (ii) the maximum capture width ratio was achieved when the relative velocity of the OWC free surface is in phase with the air chamber pressure, a condition where less reactive power is verified; (iii) the higher the compressibility in the air chamber, the higher the effect in the buoy's motions, and this may affect the selection of an optimum PTO; (iv) higher losses during inhalation processes should be expected when the spring-like effect of the air is more significant; and v) high-frequency components were detected in the OWC free surface motion in both inhalation and exhalation processes, probably due to the relative motion between the buoy and the OWC. However, these were found not to significantly affect the pneumatic chamber's air pressure.

A new compressibility factor was defined to aid in designing experimental and numerical studies or in assessing the importance of the compressibility effects on previously obtained experimental results.

#### CRediT authorship contribution statement

**J.C.C. Portillo:** Conceptualization, Methodology, Software, Experiments execution, Data curation, Formal analysis, Visualization, Writing – original draft. **J.C.C. Henriques:** Conceptualization, Software, Data

curation, Visualization, Validation, Writing – review & editing. **L.M.C. Gato:** Conceptualization, Methodology, Formal analysis, Supervision, Writing – review & editing, Validation, Funding acquisition. **A.F.O. Falção:** Conceptualization, Supervision, Formal analysis, Writing – review & editing.

### Declaration of competing interest

The authors declare that they have no known competing financial interests or personal relationships that could have appeared to influence the work reported in this paper.

### Data availability

Data will be made available on request.

### Acknowledgements

This work was funded by the Portuguese Foundation for Science and Technology (FCT) through IDMEC, under LAETA, project UIDB/50022/2020 and MIT-EXPL/SOE/0094/2019, and by Fundo Azul organisation from the Portuguese Ministry of the Sea through BlueCAO project, agreement FA/02/2017/009. The authors thank the Portuguese National Laboratory of Civil Engineering (LNEC), and especially Dr Juana Fortes, for the support, receptivity and authorisation to use the wave flume for the experiments reported in this work. The authors also acknowledge the collaboration of the University of Plymouth for lending the 1:40-scale coaxial-duct model constructed under the EU H2020 Wave Energy Transition to Future by Evolution of Engineering and Technology project (WETFEET) project with grant agreement No 641334.

### Appendix A. The compressibility factor

Eq. (1) can be rearranged to give

$$\frac{\dot{p}_a}{\rho_a} + \frac{\dot{V}}{V} = -\frac{w_t}{\rho_a V}, \quad (\text{A.1})$$

where the over dot denotes time derivative. The time derivative of the volume per unit volume can be expressed as

$$\frac{\dot{V}}{V} = \frac{-S_{owc} \dot{z}_{owc}}{-S_{owc} h_{ac}} = \frac{\dot{z}_{owc}}{h_{ac}}, \quad (\text{A.2})$$

where  $\dot{z}_{owc} = \dot{z}_2 - \dot{z}_1$  represents the relative velocity of the buoy with respect to the OWC free surface (see Fig. 1),  $h_{ac} = V/S_{owc}$  is the equivalent height of the air chamber, and  $S_{owc}$  being the OWC water-plane area.

The isentropic compression/expansion of the air in the chamber can be modelled as

$$\frac{p + p_{atm}}{\rho_a^\gamma} = \text{const}, \quad (\text{A.3})$$

where  $p$  is pressure in the chamber relative to the atmosphere  $p_{atm}$ . Taking the logarithm of both sides of Eq. (A.3) gives

$$\frac{\dot{p}_a}{\rho_a} = \frac{\dot{p}}{\gamma (p + p_{atm})}. \quad (\text{A.4})$$

Replacing Eqs. (A.2) and (A.4) in Eq. (A.1), yields

$$\frac{\dot{p}}{p + p_{atm}} = -\gamma \left( \frac{\dot{z}_{owc}}{h_{ac}} + \frac{w_t}{\rho_a V} \right). \quad (\text{A.5})$$

Considering that  $p \ll p_{atm}$  and the stiffest case occurs when  $w_t = 0$ , Eq. (A.5) reduces to

$$\frac{\dot{p}}{p_{atm}} = -\gamma \frac{\dot{z}_{owc}}{h_{ac}}. \quad (\text{A.6})$$

Scaling the relative pressure  $p$  with the pressure amplitude  $P$ , the relative displacement  $z_{owc}$  by the motion amplitude  $Z_{owc}$ , and the time  $t$  by the wave period  $T$ , we get

$$\frac{P}{p_{atm}} \frac{dp^*}{dt^*} = -\gamma \frac{Z_{owc}}{h_{ac}} \frac{dz_{owc}^*}{dt^*}, \quad (\text{A.7})$$

where  $p^* = p/P$ ,  $z_{owc}^* = z_{owc}/Z_{owc}$  and  $t^* = t/T$ . The compressibility factor  $\mathcal{X}$  can be defined as the ratio of the scale of the pressure fluctuations over the scale of the relative OWC velocity, such that

$$\mathcal{X} \frac{\frac{dp^*}{dt^*}}{\frac{dz_{owc}^*}{dt^*}} = -1, \quad (\text{A.8})$$

where

$$\mathcal{X} = \frac{P}{\gamma p_{atm}} \frac{h_{ac}}{Z_{owc}}. \quad (\text{A.9})$$

The compressibility factor  $\mathcal{X}$  can be viewed as a generalisation of  $\Gamma$  parameter presented in Ref. [31]. Since the compressibility factor is dimensionless, its value is independent of the scale.

### Appendix B. Equivalency between biradial air turbine size and orifice diameter

The model-scale aerodynamic modelling of an air turbine is discussed in Ref. [31]. Here we show how to determine the orifice area that simulates the pressure drop across an ideal impulse turbine. Neglecting the effects of the variations of the Reynolds number (the Reynolds number is generally large enough to justify that assumption) and Mach number, the air turbine dimensionless flow rate

$$\Psi = \frac{p}{\rho_{a,in} \Omega^2 d_t^2}, \quad (\text{B.1})$$

is a function of the dimensionless pressure head

$$\Phi = \frac{q_t}{\Omega d_t^3}, \quad (\text{B.2})$$

where  $\Omega$  represents the turbine rotational speed,  $d_t$  is the turbine rotor diameter,  $\Delta p$  is the pressure drop,  $q_t$  volumetric airflow rate through the turbine, and  $\rho_{a,in}$  is the air density at inlet stagnation conditions.

An ideal biradial (impulse) turbine has a quadratic relationship between the dimensionless pressure head and the dimensionless volumetric rate

$$\Psi = \kappa_t \Phi^2. \quad (\text{B.3})$$

Here  $\kappa_t$  is a constant that depends on the turbine geometry but not on its size. The previous relationship can be rewritten as

$$q_t = \text{sign}(p) \frac{d_t^2}{\sqrt{\kappa_t}} \sqrt{\frac{|p|}{\rho_{a,in}}}. \quad (\text{B.4})$$

Note that (B.4) does not depend on the turbine rotational speed. On the other hand, the flow rate across an orifice can be written as

$$q_{or} = \text{sign}(p) C_d A_{or} \sqrt{2 \frac{|p|}{\rho_a}}, \quad (\text{B.5})$$

where  $C_d$  is the so-called discharge coefficient,  $A_{or}$  is the orifice area, and  $\rho_a$  is the air density. Assuming that  $\rho_{a,in} \approx \rho_a$  and equating  $q_t = q_{or}$  results in an orifice area of

$$A_{or} = \frac{d_t^2}{\sqrt{2\kappa_t} C_d}. \quad (\text{B.6})$$

As shown in [31], the turbine model scales-down as

$$d_{t,M} = d_{t,F} \lambda \delta^{-1/4}, \quad (\text{B.7})$$

where  $d_{t,M}$  and  $d_{t,F}$  are the turbine rotor diameter of the model and prototype (full scale), respectively; with  $\delta = \rho_{w,M}/\rho_{w,F}$ , as presented in Section 2.



## References

- [1] Barstow S, Mørk G, Mollison D, Cruz J. The wave energy resource. In: Cruz J, editor. *Ocean wave energy: current status and future perspectives*. Berlin: Springer; 2008, p. 93–132. [http://dx.doi.org/10.1007/978-3-540-74895-3\\_4](http://dx.doi.org/10.1007/978-3-540-74895-3_4).
- [2] Kofoed JP. The wave energy sector. In: Pecher A, Kofoed JP, editors. *Handbook of ocean wave energy*. Cham: Springer International Publishing; 2017, p. 17–42. [http://dx.doi.org/10.1007/978-3-319-39889-1\\_2](http://dx.doi.org/10.1007/978-3-319-39889-1_2).
- [3] Drew B, Plummer AR, Sahinkaya MN. A review of wave energy converter technology. *Proc Inst Mech Eng A J Power Energy* 2009;223:882–902. <http://dx.doi.org/10.1243/09576509JPE782>.
- [4] Falcão AFO. Wave energy utilization: A review of the technologies. *Renew Sustain Energy Rev* 2010;14:899–918. <http://dx.doi.org/10.1016/j.rser.2009.11.003>.
- [5] Lopez I, Andreu J, Ceballos S, de Alegria M, Kortabarria I. Review of wave energy technologies and the necessary power-equipment. *Renew Sustain Energy Rev* 2013;22:413–34. <http://dx.doi.org/10.1016/j.rser.2013.07.009>.
- [6] Falcão AFO, Henriques JCC. Oscillating-water-column wave energy converters and air turbines: A review. *Renew Energy* 2016;85:1391–424. <http://dx.doi.org/10.1016/j.renene.2015.07.086>.
- [7] Wells AA. Fluid driven rotary transducer. 1976, British Patent Spec No. 1595700.
- [8] Curran R, Gato LMC. The energy conversion performance of several types of Wells turbine designs. *Proc Inst Mech Eng A J Power Energy* 1997;221:133–45. <http://dx.doi.org/10.1243/09576509JPE1537051>.
- [9] Gato LMC, Carrelhas AAD, Cunha AFA. Performance improvement of the axial self-rectifying impulse air-turbine for wave energy conversion by multi-row guide vanes: Design and experimental results. *Energy Convers Manage* 2021;243:114305. <http://dx.doi.org/10.1016/j.enconman.2021.114305>.
- [10] Falcão AFO, Gato LMC. Turbine with radial inlet and outlet rotor for use in bidirectional flows. 2011.
- [11] Falcão AFO, Gato LMC, Henriques JCC, Borges JE, Pereira B, Castro F. A novel twin-rotor radial-inflow air turbine for oscillating-water-column wave energy converters. *Energy* 2015;93:2116–25. <http://dx.doi.org/10.1016/j.energy.2015.10.046>.
- [12] Scialò A, Henriques JCC, Malara G, Falcão AFO, Gato LMC, Arena F. Power take-off selection for a fixed U-OWC wave power plant in the Mediterranean Sea: The case of Rocella Jonica. *Energy* 2021;215:119085. <http://dx.doi.org/10.1016/j.energy.2020.119085>.
- [13] Ferreira DN, Gato LMC, Eça L, Henriques JCC. Aerodynamic analysis of a biradial turbine with movable guide-vanes: Incidence and slip effects on efficiency. *Energy* 2020;200:117502. <http://dx.doi.org/10.1016/j.energy.2020.117502>.
- [14] Carrelhas AAD, Gato LMC, Henriques JCC, Falcão AFO. Experimental study of a self-rectifying biradial air turbine with fixed guide-vanes arranged into concentric annular rows. *Energy* 2020;198:117211. <http://dx.doi.org/10.1016/j.energy.2020.117211>.
- [15] Fox BN, Gomes RPF, Gato LMC. Analysis of oscillating-water-column wave energy converter configurations for integration into caisson breakwaters. *Appl Energy* 2021;295:117023. <http://dx.doi.org/10.1016/j.apenergy.2021.117023>.
- [16] Henriques JCC, Portillo JCC, Sheng W, Gato LMC, Falcão AFO. Dynamics and control of air turbines in oscillating-water-column wave energy converters: Analyses and case study. *Renew Sustain Energy Rev* 2019;112:571–89. <http://dx.doi.org/10.1016/j.rser.2019.05.010>.
- [17] Gato LMC, Henriques JCC, Carrelhas AAD. Sea trial results of the biradial and Wells turbines at Mutriku wave power plant. *Energy Convers Manage* 2022;268:115936. <http://dx.doi.org/10.1016/j.enconman.2022.115936>.
- [18] Arena F, Romolo A, Malara G, Ascanelli A. On design and building of a U-OWC wave energy converter in the mediterranean sea: A case study. In: *Proceedings of the ASME 2013 32th international conference on ocean, offshore and arctic engineering*. Volume 8: Ocean renewable energy. Nantes, France. June 9–14. 2013. <http://dx.doi.org/10.1115/OMAE2013-11593>.
- [19] Sheng W. Power performance of BBDB OWC wave energy converters. *Renew Energy* 2019;132:709–22. <http://dx.doi.org/10.1016/j.renene.2018.07.111>.
- [20] Portillo JCC, Reis PF, Henriques JCC, Gato LMC, Falcão AFO. Backward bent-duct buoy or frontward bent-duct buoy? Review, assessment and optimisation. *Renew Sustain Energy Rev* 2019;112:353–68. <http://dx.doi.org/10.1016/j.rser.2019.05.026>.
- [21] Gomes RPF, Henriques JCC, Gato LMC, Falcão AFO. Hydrodynamic optimization of an axisymmetric floating oscillating water column for wave energy conversion. *Renew Energy* 2012;44:328–39. <http://dx.doi.org/10.1016/j.renene.2012.01.105>.
- [22] Carrelhas AAD, Gato LMC, Henriques JCC, Falcão AFO, Varandas J. Test results of a 30 kW self-rectifying biradial air turbine-generator prototype. *Renew Sustain Energy Rev* 2019;109:187–98. <http://dx.doi.org/10.1016/j.rser.2019.04.008>.
- [23] OceanEnergy. OceanEnergy: A world of power. 2022, URL <https://oceanenergy.ie>. [Accessed 09 August 2022].
- [24] Portillo JCC, Collins KM, Gomes RPF, Henriques JCC, Gato LMC, Howey BD, et al. Wave energy converter physical model design and testing: The case of floating oscillating-water-columns. *Appl Energy* 2020;278:115638. <http://dx.doi.org/10.1016/j.apenergy.2020.115638>.
- [25] Falcão AFO, Henriques JCC. The spring-like air compressibility effect in oscillating-water-column wave energy converters: Review and analyses. *Renew Sustain Energy Rev* 2019;112:483–98. <http://dx.doi.org/10.1016/j.rser.2019.04.040>.
- [26] López I, Carballo R, Taveira-Pinto F, Iglesias G. Sensitivity of OWC performance to air compressibility. *Renew Energy* 2020;145:1334–47. <http://dx.doi.org/10.1016/j.renene.2019.06.076>.
- [27] Folley M, Whittaker TJT. The effect of plenum chamber volume and air turbine hysteresis on the optimal performance of oscillating water columns. In: *Proceedings of the 24th international conference on ocean, offshore and arctic engineering*, Halkidiki, Greece, Paper No. OMAE2005-67070. 2005. <http://dx.doi.org/10.1115/OMAE2005-67070>.
- [28] Sheng W, Lewis A. Wave energy conversion of oscillating water column devices including air compressibility. *J Renew Sustain Energy* 2016;8(5):054501. <http://dx.doi.org/10.1063/1.4963237>.
- [29] Elhanafi A, Macfarlane G, Fleming A, Leong Z. Scaling and air compressibility effects on a three-dimensional offshore stationary OWC wave energy converter. *Appl Energy* 2017;189:1–20. <http://dx.doi.org/10.1016/j.apenergy.2016.11.095>.
- [30] Portillo JCC, Henriques JCC, Gomes RPF, Gato LMC, Falcão AFO. On the array of wave energy converters: The case of the coaxial-duct OWC. In: *Proceedings of the 37th international conference on ocean, offshore and arctic engineering*, Madrid, Paper No. OMAE2018-78022. 2018.
- [31] Falcão AFO, Henriques JCC. Model-prototype similarity of oscillating-water-column wave energy converters. *Int J Mar Energy* 2014;6:18–34. <http://dx.doi.org/10.1016/j.ijome.2014.05.002>.
- [32] Liu Z, Xu C, Kim K, Choi J, Hyun B. An integrated numerical model for the chamber-turbine system of an oscillating water column wave energy converter. *Renew Sustain Energy Rev* 2021;149:111350. <http://dx.doi.org/10.1016/j.rser.2021.111350>.
- [33] Falcão AFO, Henriques JCC, Gomes RPF, Portillo JCC. Theoretically based correction to model test results of OWC wave energy converters to account for air compressibility effect. *Renew Energy* 2022;198:41–50. <http://dx.doi.org/10.1016/j.renene.2022.08.034>.
- [34] Sarmiento AJNA, de O. Falcão AF. Wave generation by an oscillating surface-pressure and its application in wave-energy extraction. *J Fluid Mech* 1985;150:467–85. <http://dx.doi.org/10.1017/S0022112085000234>.
- [35] Goda Y, Suzuki Y. Estimation of incident and reflected waves in random wave experiments. In: *Proceedings of 15th international conference on coastal engineering*, ASCE, Honolulu, USA; 1976, p. 828–45. <http://dx.doi.org/10.1061/9780872620834.048>.
- [36] Mansard E, Funke E. The measurement of incident and reflected spectra using a least squares method. In: *Coastal engineering*. 1980, p. 154–72. <http://dx.doi.org/10.1061/9780872622647.008>.
- [37] Sheng W, Thiebaud F, Babuchon M, Brooks J, Lewis A, Alcorn R. Investigation to air compressibility of oscillating water column wave energy converters. In: *Proceedings of the 32nd international conference on ocean, offshore and arctic engineering*, Nantes, France, Paper No. OMAE2013-10151. 2013. <http://dx.doi.org/10.1115/OMAE2013-10151>.
- [38] Henriques JCC, Portillo JCC, Gato LMC, Gomes RPF, Ferreira DN, Falcão AFO. Design of oscillating-water-column wave energy converters with an application to self-powered sensor buoys. *Energy* 2016;112:852–67. <http://dx.doi.org/10.1016/j.energy.2016.06.054>.
- [39] Falcão J. *Ocean waves and oscillating systems*. Cambridge, UK: Cambridge University Press; 2002.
- [40] Greaves D. 3. Wave energy technology. In: Greaves D, Iglesias G, editors. *Wave and tidal energy*. Hoboken, NJ: Wiley; 2018, p. 52–104.
- [41] Simonetti I, Cappiotti L, Elsafti H, Oumeraci H. Evaluation of air compressibility effects on the performance of fixed OWC wave energy converters using CFD modelling. *Renew Energy* 2018;119:741–53. <http://dx.doi.org/10.1016/j.renene.2017.12.027>.
- [42] Weber J. *Optimisation of the hydrodynamic-aerodynamic coupling of an oscillating water column wave energy device* (Ph.D. thesis), University College Cork, Ireland; 2006.
- [43] Ibrahim RA. *Liquid sloshing dynamics: theory and applications*. Cambridge University Press; 2005. <http://dx.doi.org/10.1017/CBO9780511536656>.